IOP PUBLISHING PHYSICS IN MEDICINE AND BIOLOGY

Phys. Med. Biol. **53** (2008) 6673–6694 doi:10.1088/0031-9155/53/23/003

Full-field laser–Doppler imaging and its physiological significance for tissue blood perfusion

T Binzoni[1,2] **and D Van De Ville**[3,4]

[1] Département des Neurosciences Fondamentales, University of Geneva, Switzerland
[2] Département de l'Imagerie et des Sciences de l'Information Médicale, Geneva University Hospitals, Switzerland
[3] Biomedical Imaging Group, Ecole Polytechnique Fédérale de Lausanne (EPFL), Switzerland

E-mail: Tiziano.Binzoni@medecine.unige.ch

Received 4 August 2008, in final form 16 September 2008
Published 7 November 2008
Online at stacks.iop.org/PMB/53/6673

Abstract

Using Monte Carlo simulations for a semi-infinite medium representing a skeletal muscle tissue, it is demonstrated that the zero- and first-order moments of the power spectrum for a representative pixel of a full-field laser–Doppler imager behave differently from classical laser–Doppler flowmetry. In particular, the zero-order moment has a very low sensitivity to tissue blood volume changes, and it becomes completely insensitive if the probability for a photon to interact with a moving red blood cell is above 0.05. It is shown that the loss in sensitivity is due to the strong forward scatter of the propagating photons in biological tissues (i.e., anisotropy factor $g = 0.9$). The first-order moment is linearly related to the root mean square of the red blood cell velocity (the Brownian component), and there is also a positive relationship with tissue blood volume. The most common physiological interpretation of the first-order moment is as tissue blood volume times expectation of the blood velocity (in probabilistic terms). In this sense, the use of the first-order moment appears to be a reasonable approach for qualitative real-time blood flow monitoring, but it does not allow us to obtain information on blood velocity or volume independently. Finally, it is shown that the spatial and temporal resolution trade-off imposed by the CMOS detectors, used in full-field laser–Doppler hardware, may lead to measurements that vary oppositely with the underlying physiological quantities. Further improvements on detectors' sampling rate will overcome this limitation.

(Some figures in this article are in colour only in the electronic version)

[4] Address for correspondance: Centre Médical Universitaire, 1, r. Michel-Servet, Département des Neurosciences Fondamentales, 1211 Genéve 4, Switzerland.

1. Introduction

During the past decades, non-invasive laser–Doppler and laser speckle based imaging techniques (Briers 2001, 2007, Vennemann *et al* 2007) have attracted large interest of many research laboratories and of the medical community in particular. The development of the charge-coupled device (CCD) and complementary metal-oxide-semiconductor (CMOS) digital technology has allowed us to conceive real-time tissue blood perfusion imagers. These imagers do not necessitate direct contact with the tissue under investigation (ideal for the surgical environment), are non-invasive and can be utilized on humans. In particular, fast sampling rate CMOS sensors (Fossum 1997, Hoffman *et al* 2005) seem to have the greatest potential for the conception of a new class of full-field laser–Doppler imagers (FFLDI), and some prototypes have already been proposed (Serov *et al* 2002, 2005, Serov and Lasser 2005).

While the sensitivity and sampling speed of FFLDI can expect to gain from ongoing technological developments, there are still open theoretical questions to resolve. The analytical models and the numerical simulations for 'classical' laser–Doppler hardware may intuitively be reduced to a short-distance source–detector configuration problem (Briers 2001). However, the FFLDI illuminates the whole observed tissue region with a very large spot of light. This can be seen as an infinite number of source–detector couples with the photons simultaneously interacting in a complex manner over all possible paths (for schematic representations of 'classical' laser–Doppler and FFLDI see figure 1). Consequently, there is no guarantee that classical algorithms to extract blood volume and flow information (e.g. analysis of the moments of the power spectrum, Bonner and Nossal 1981) actually still work with FFLDI. Analytical modeling of FFLDI using light transport and the laser–Doppler theory becomes too complex, if not impossible. This complexity may be explained by the fact that a given FFLDI detector pixel captures photons that simultaneously originate from sources located over a wide range of distances, going from very short (e.g. 1 mm) to very large (e.g. 20 mm). On one hand, the presence of short photon paths, due to the particular values of the scattering and absorption coefficients in biological tissues, makes it theoretically impossible to use the diffusion approximation of the radiative transport equation to facilitate the calculations. On the other hand, photons that traveled large distances do not allow for the single scattering approximation because they may interact many times with the moving particles before reaching the detector. These difficulties prevent us from deriving an explicit analytical model that would allow us to investigate the behavior of FFLDI signals as the tissue's physiological parameters vary. Therefore, the use of numerical simulations is probably the most efficient strategy to approach the problem.

In an attempt to clarify some of the highlighted problems, the aim of the present work is to (1) numerically simulate general FFLDI working on a tissue phantom with known optical and physiological parameters, (2) study the relationship existing between the moments of the obtained power spectra and the physiological parameters, such as the tissue blood volume or the blood velocity and (3) investigate the influence of the technical constraints imposed by the CMOS sensors on the obtained measurements and compare them with the theoretical exact values. The results not only contribute to a better understanding of FFLDI, but can also serve as guidelines to the experimentalist.

2. Material and methods

2.1. Virtual tissue phantom and blood perfusion imager

The tissue phantom was represented by a homogeneous $2500 \times 2500 \times 2500$ mm^3 cube. Considering the huge amount of time necessary to make the simulations (see e.g. the legend

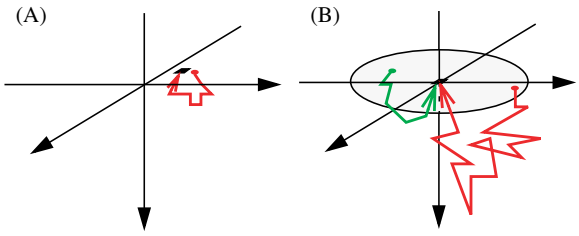

Figure 1. (A) Representation of a 'classical' laser–Doppler source–detector geometry (not to scale) where the light source (red point; gray in the non-electronic version of the manuscript) is close to the detection region (black square). One photon path is reported as an example. (B) Representation of a full-field laser–Doppler geometry (not to scale) where the light source is a large circular region. Two representative photon paths (red and green) starting from different points within the source and reaching the detector (black square) are reported.

of figure 11), we were obliged to restrict the choice of the optical parameters. The absorption coefficient (μ_a), the reduced scattering coefficient (μ_s'), the refractive index (n) and the wavelength were set to 0.025 mm^{-1}, 0.5 mm^{-1}, 1.4 and 800 nm, respectively, for all the simulations. These parameters are representative of human skeletal muscle (Zaccanti *et al* 1995, Torricelli *et al* 2004, Couvoisier 2006) in the case of blood perfusion monitoring of a flap during surgical soft tissue reconstruction. The refractive index for the air was set to 1. The anisotropy parameter (g) was set to 0 or 0.9 (Liebert *et al* 2006, 2007), depending on the simulation (see below).

The light source of the full-field imager was a uniform laser spot of 30 mm diameter, perpendicularly projected and centered on one of the faces of the cube. The detector was represented by a pixel located at the center of the same face where the light source was illuminating (see figure 1(B)). All the photons reaching the detector were taken into account independently of the detection angle. The emission angle of the photons (before reaching the detector) is determined by the last scattering event, and a reasonable assumption is that just before this event the direction of the photons is already completely randomized. In particular, the emission angle is independent of the photon's precedent history and of the accumulated Doppler shift. In practice, all the directions contain the same frequency information, and this is the reason why they can be mixed. The advantage is a gain in the signal-to-noise ratio. The position and the size of this pixel are not that critical because the size of the cube and the light source are relatively very large. Specifically, a small shift of a few millimeters of the detector pixel produces exactly the same numerical results for such a homogeneous sample (Binzoni *et al* 2008b). This fact allows one to improve the signal-to-noise ratio of the simulations by taking the mean value on several pixels covering in the present case a total surface of $S = 6 \times 6$ mm^2.

2.2. Monte Carlo method and generation of the power spectrum

Simulation of photon transport into the tissue using a Monte Carlo technique is a well-established approach. Here, we rely on a previously published implementation (Binzoni *et al* 2008a, 2008b), where we extended the original code with the laser–Doppler component. The algorithm was implemented on a cluster of 8 node PC (3 GHz, Intel, Pentium 4) allowing distributed calculations (Kirkby and Delpy 1997). Implicit photon capture variance reduction (Wang *et al* 1995) and roulette termination (Sobol 1975) techniques were deployed. The final weight of the photon packet reaching the detection region-of-interest with angular frequency

ω and direction $\hat{k}$ was $W(\omega, \hat{k})$. For the roulette technique, the trigger value was $W < 10^{-4}$ and the photon packet had a chance $1/10$ to survive with a new weight, $10W$ (the initial weight was always set to $W = 1$). The photon packet steps were generated by means of the variable step size method (Prahl *et al* 1989). The model describing the change of the photon packet direction after each collision was represented by the Henyey–Greenstein probability density function (Henyey and Greenstein 1941) independently of the fact that the scatterer was a moving particle or not (Soelkner *et al* 1997, Kienle 2001). Reflection of the photon packets on the boundaries was treated as an all-or-none problem by using the probability density functions derived from the Snell–Descartes law and Fresnel's formulae.

The laser–Doppler shift for each individual photon (packet) was computed by means of the method published in Soelkner *et al* (1997) (see equation (1)). After each scattering event it was decided if the scatterer was a moving particle by sampling a uniform random number $\xi \in [0, 1]$ and by defining the probability of having a moving particle $P_{\text{move}} \in [0, 1]$. The parameter P_{move} is classically interpreted for obvious reasons as proportional to the tissue blood volume, and we will also use this terminology. The model describing the velocity distribution ($\vec{V}$, mm s^{-1}) of the moving particles was represented by the probability density function $p(\vec{V})$ (see below). Thus, once $\vec{V}$ was generated using the law given by $p(\vec{V})$, the laser–Doppler frequency shift ($\Delta\nu_q$, Hz) for the qth scattering event with a moving particle was computed as (Soelkner *et al* 1997)

$$\Delta\omega_q = 2\pi\,\Delta\nu_q = \frac{(\vec{k}_s - \vec{k}_i)\vec{V}_q}{2\pi}, \tag{1}$$

where $\vec{k}_i$ and $\vec{k}_s$ are the wave vectors for the input and scattered light and

$$\|\vec{k}_s\| = \|\vec{k}_i\| = \frac{2\pi n}{\lambda} \tag{2}$$

with $\lambda = 800$ nm. Thus, the angular frequency of the photon packet reaching the detection pixel, with weight $W(\omega, \hat{k})$ and direction $\hat{k}$, was expressed as

$$\omega = \omega_0 + \sum_{q=1}^{M} \Delta\omega_q = \omega_0 + \Delta\omega, \tag{3}$$

where M is the total number of scattering events with a moving particle and $\omega_0 = 2\pi c/\lambda$. The above procedure was repeated for $N = 1\times10^6$ photon packets for each of the simulations in this work, if it is not differently specified. The $\omega - W(\omega, \hat{k})$ couples were stored in a histogram form, $\omega - W_{\text{tot}}(\omega)$, where $W_{\text{tot}}(\omega)$ was the sum of all $W(\omega, \hat{k})$ having the corresponding angular frequency falling in the interval $[\omega, \omega + \delta\omega]$ with $\delta\omega/2\pi \approx 19.53$ Hz independently of the direction $\hat{k}$. For a very high number of photons, we can think of ω as a continuous-domain variable. Intuitively, $W_{\text{tot}}(\omega)$ may be seen as the 'optical spectrum' obtained with an idealized spectrophotometer which would allow us to observe the optical angular frequencies with an extremely high resolution. In practice, the FFLDI is able to detect only the 'beating' component which has very low angular frequencies (i.e., $\Delta\omega = \omega - \omega_0$). This 'beating' component is usually represented as a power spectrum ($S(\Delta\omega)$) and was computed by using the classical method as published by de Mul *et al* (1995) and previously proposed by Forrester (1961):

$$S(\Delta\omega) = a\int_0^\infty W_{\text{tot}}(\omega_1)\,W_{\text{tot}}(\omega_1 + \Delta\omega)\,\mathrm{d}\omega_1, \tag{4}$$

where the proportionality constant a is not known, and for this reason $S(\Delta\omega)$ was expressed in arbitrary units (a.u.). Thus, the last operation represented by equation (4) takes into account

interference phenomena generated by the interaction between the different photons. It must be noted that $\Delta\omega$ may have negative values; however, the FFLDI is not able to detect negative frequencies and they appear in the spectrum as positive. Thus, in practice the resulting power spectrum, $P(\Delta\omega)$ (a.u.), for $\Delta\omega \geqslant 0$ was finally obtained as

$$P(\Delta\omega) = \begin{cases} S(0), & \text{if} \quad \Delta\omega = 0 \\ S(-|\Delta\omega|) + S(|\Delta\omega|) & \text{if} \quad \Delta\omega > 0. \end{cases} \tag{5}$$

2.3. The probability density function for the tissue blood velocity

The probability density function (p) allowing us to randomly generate the velocity ($\vec{V}$) of a moving particle (red blood cell) was defined as

$$p(\vec{V}) = \prod_{\alpha\in\{x,y,z\}} p_\alpha(V_\alpha), \tag{6}$$

where V_x, V_y and V_z are the $\vec{V}$ components. The probability density function for each V_α was (Zhong *et al* 1998, Binzoni *et al* 2004, 2006)

$$p_\alpha(V_\alpha) = \left(\frac{3}{2\langle V^2_{\text{Brown}}\rangle}\right)^{1/2} \frac{1}{\pi^{1/2}} \left(\mathrm{e}^{-\frac{3}{2\langle V^2_{\text{Brown}}\rangle}(V_\alpha - V_{\text{trans},\alpha})^2}\right), \tag{7}$$

where the constant $\langle V^2_{\text{Brown}}\rangle^{1/2} \in [0, \infty)$ (mm s^{-1}) represents the root mean square of the particle velocity due to the 'Brownian' motion. The constants $V_{\text{trans},\alpha} \in (-\infty, \infty)$ (mm s^{-1}) represent the components of the particle's global translational velocity ($\vec{V}_{\text{trans}}$). This function is very general because, in addition to the typical case of the 'Brownian motion', it also allows us to describe tissues where the blood flow may be strongly directional, such as for the skeletal muscle where vessels run along the direction of the muscle cells. For a better explanation of this point see the 'Discussion' section. The probability density function (p_n) for $\|\vec{V}\|$ may be derived from equations (6) and (7) by following the procedure of Zhong *et al* (1998) which gives

$$p_n(\|\vec{V}\|) = \left(\frac{3}{2\langle V^2_{\text{Brown}}\rangle}\right)^{1/2} \frac{\|\vec{V}\|}{\sqrt{\pi}\|\vec{V}_{\text{trans}}\|} \left\{ \exp\left[-\frac{3}{2\langle V^2_{\text{Brown}}\rangle}(\|\vec{V}\| - \|\vec{V}_{\text{trans}}\|)^2\right] - \exp\left[-\frac{3}{2\langle V^2_{\text{Brown}}\rangle}(\|\vec{V}\| + \|\vec{V}_{\text{trans}}\|)^2\right]\right\}, \tag{8}$$

where $\|\|$ is the ℓ_2 norm of the vector.

The method originally proposed by Witt (1977) has been used to simulate the random event for which the variable V_α falls with the probability $p_\alpha(V_\alpha)\,\mathrm{d}V_\alpha$ in the interval $[V_\alpha, V_\alpha + \mathrm{d}V_\alpha]$. For the present purpose, it was also necessary to take into account the fact that in real tissues, the velocity V_α covers a finite range of possible values, i.e., $V_\alpha \in (V_{\alpha,\min}, V_{\alpha,\max})$ and $V_{\alpha,\min} < V_{\alpha,\max} \in (-\infty, \infty)$. As a consequence, the relation between the cumulative distribution function (right-hand side of equation (9)) and ξ_α was expressed as

$$\xi_\alpha = \frac{\int_{V_{\alpha,\min}}^{V_\alpha} p_\alpha(V'_\alpha)\,\mathrm{d}V'_\alpha}{\int_{V_{\alpha,\min}}^{V_{\alpha,\max}} p_\alpha(V'_\alpha)\,\mathrm{d}V'_\alpha}, \tag{9}$$

which holds for each coordinate α independently. The denominator appearing in equation (9) is the normalization factor for a given $V_{\alpha,\min}$ and $V_{\alpha,\max}$. In practice, the cumulative distribution function of $p_\alpha(V_\alpha)$ allows us to build a look-up table that provides a one-to-one correspondence

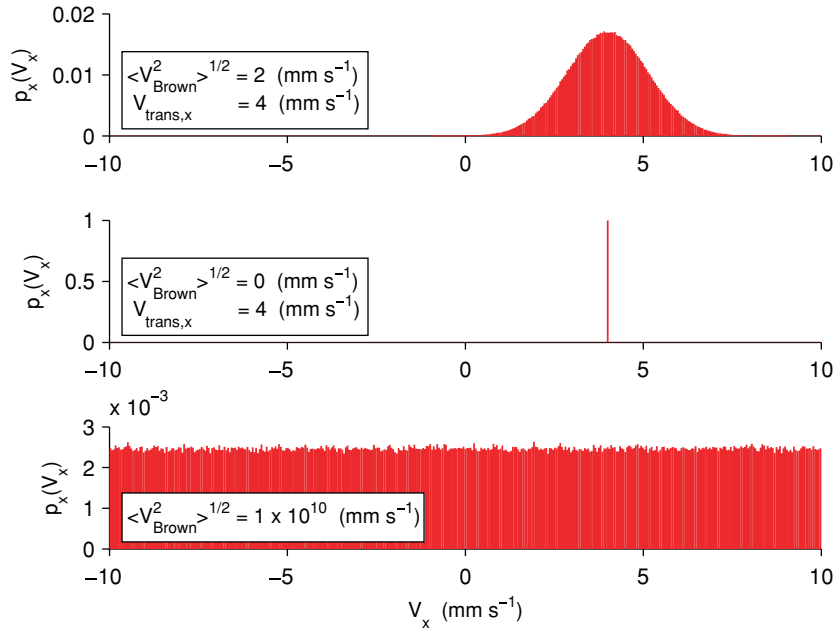

Figure 2. Probability density function ($p_x(V_x)$) for the x-component (V_x) of the velocity vector $\bar{V}$ computed by means of equation (10). A total of 1×10^6 realizations for $\xi_x \in [0, 1]$ uniformly distributed random variable were used for the bar graphs. The three different sets of parameters $\langle V^2_{\text{Brown}}\rangle^{1/2}$ and $V_{\text{trans},x}$ utilized to define the three different examples for $p_x(V_x)$ are directly reported on the corresponding panels.

between a uniformly distributed random number $\xi_\alpha \in [0, 1]$ and a realization of V_α. Direct numerical integration of equations (7) and (9) may become numerically instable for some particular $\langle V^2_{\text{Brown}}\rangle^{1/2}$ and $V_{\text{trans},\alpha}$ values. Thus, the following analytical form directly derived from equations (7) and (9) is preferable for the Monte Carlo simulations:

$$\xi_\alpha = \begin{cases} \dfrac{\operatorname{erfc}\left(\frac{V_{\alpha,\min} - V_{\text{trans},\alpha}}{(2\langle V^2_{\text{Brown}}\rangle/3)^{1/2}}\right) - \operatorname{erfc}\left(\frac{V_\alpha - V_{\text{trans},\alpha}}{(2\langle V^2_{\text{Brown}}\rangle/3)^{1/2}}\right)}{\operatorname{erfc}\left(\frac{V_{\alpha,\min} - V_{\text{trans},\alpha}}{(2\langle V^2_{\text{Brown}}\rangle/3)^{1/2}}\right) - \operatorname{erfc}\left(\frac{V_{\alpha,\max} - V_{\text{trans},\alpha}}{(2\langle V^2_{\text{Brown}}\rangle/3)^{1/2}}\right)} \\ \dfrac{1}{2}; \qquad \text{if} \quad \left(\langle V^2_{\text{Brown}}\rangle = 0\right) \wedge (V_\alpha = V_{\text{trans},\alpha}), \end{cases} \tag{10}$$

where erfc is the complementary error function. It must be noted that the Matlab language used to implement the code utilizes the IEEE arithmetic representation, and thus it allows us to correctly manage the presence of infinities and 0/0 terms. In figure 2 are shown some representative velocity distributions that are possible to obtain by means of the look-up table derived from equation (10).

2.4. Derivation of the perfusion/speed related parameters from the power spectrum

The classical approach utilized to extract physiological information from $P(\Delta\omega)$, especially if one needs a real-time treatment (Serov and Lasser 2005), is to compute the zero- ($\langle\omega^0\rangle$) and the first-order ($\langle\omega^1\rangle$) moments (Bonner and Nossal 1981), which are defined as

$$\langle\omega^p\rangle = \int_0^\infty \omega^p P(\Delta\omega)\, \mathrm{d}(\Delta\omega), \qquad p \in \{0, 1\}. \tag{11}$$

The DC spike (no Doppler shift) is not taken into account for the moment calculation, as is the case for real-world laser–Doppler instrumentation. For a simple source–detector laser–Doppler flowmetry setup, $\langle\omega^0\rangle$ is proportional to the (moving) tissue blood volume with a reasonable approximation, whereas $\langle\omega^1\rangle$ is proportional to the tissue blood flow. It remains to be demonstrated that this rule also holds for FFLDI, and this is one of the aims of this work. Note that here the words 'flow' or 'perfusion' are used with an equivalent meaning. Probably, for the case $\left\langle V^2_{\text{Brown}}\right\rangle^{1/2} = 0$, it would be better to speak about 'flow', but for $\vec{V}_{\text{trans}} = 0$, the term 'perfusion' might be better adapted. In any case, this choice has strictly no consequence for the present results or for their interpretation.

2.5. Simulations settings for the full field laser–Doppler imager configuration

To cover a reasonable number of physiological situations, the power spectra were generated for all the possible combinations of the following parameters: (1) $g = 0$, $P_{\text{move}} \in \{0.025, 0.05, 0.075, 0.1, 0.125, 0.15\}$, $\left\langle V^2_{\text{Brown}}\right\rangle^{1/2} \in \{0, 1, 2, 3, 4\}$, $V_{\text{trans},x} \in \{0, 1, 2, 3, 4\}$ and (2) $g = 0.9$, $P_{\text{move}} \in \{0.025, 0.05, 0.075, 0.1, 0.125, 0.15\}$, $\left\langle V^2_{\text{Brown}}\right\rangle^{1/2} \in \{1, 2, 3, 4\}$ and $V_{\text{trans},x} \in \{0, 1, 2, 3, 4\}$. The fixed parameters were $V_{x,\text{min}} = -10$, $V_{x,\text{max}} = 10$, $V_{\text{trans},y} = 0$ and $V_{\text{trans},z} = 0$. Obviously, the combination $\left\langle V^2_{\text{Brown}}\right\rangle^{1/2} = V_{\text{trans},x} = 0$ was not used because this would mean no blood speed and thus by definition no laser–Doppler signal. The particular choice of the $\vec{V}_{\text{trans}}$ direction along the positive x-axis direction implies that the bulk translational movement of the blood is parallel to the phantom surface where the laser light source is projected. The chosen P_{move} values cover the typical range of the skeletal muscle (Kienle 2001).

2.6. Simulations settings for a 'classical' laser–Doppler flowmeter

As explained in the 'Introduction' section, one of the aims of the present work was to investigate if the algorithms (equation (11)) used in 'classical' LDF can also be successfully applied to FFLDI. To facilitate the reading of the manuscript and the comparison between the two situations, a series of Monte Carlo simulations have also been performed for the 'classical' LDF configuration on the same cubic phantom. Considering that this is a well-known matter, these results will be presented only in the 'Discussion' section. For 'classical' LDF, it is understood as a simple point source–detector configuration (see figure 1A). The cylindrical symmetry of the problem typically allows us to treat the problem as a point source and an annular detector (75 μm width). The interoptode spacing (0.5 mm) was defined as the distance between the source and the middle point of the annular detector. The number of photon packets was $N = 3 \times 10^6$. All the remaining optical and physiological parameters were the same as for the FFLDI simulations.

3. Results

In figure 3(A) are reported the $\langle\omega^0\rangle$ values obtained from $P(\Delta\omega)$ as a function of a pure translational velocity (i.e., $\langle V^2_{\text{Brown}}\rangle = 0$) for the red blood cells. The different markers correspond to different tissue blood volumes (P_{move}) and the photon scattering events were considered to be isotropic ($g = 0$). As in the case for classical laser–Doppler instrumentation, we observe that as a first approximation $\langle\omega^0\rangle$ (classically related to the tissue blood volume) is independent of $V_{\text{trans},x}$, but that it increases non-linearly when P_{move} increases. To provide

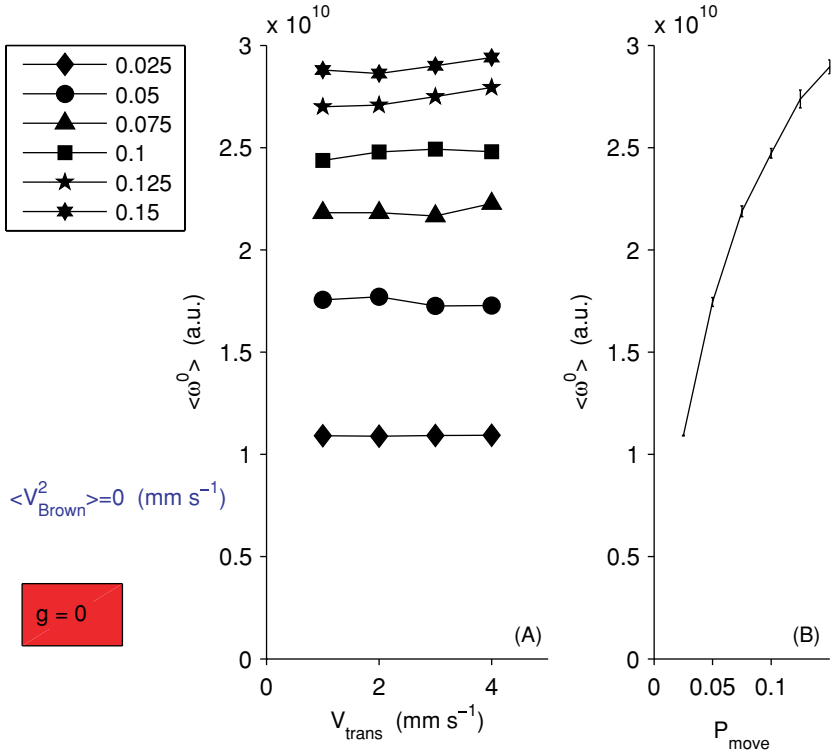

Figure 3. (A) Zero-order moment, $\langle\omega^0\rangle$, of the FFLDI power spectrum of one representative pixel, $P(\Delta\omega)$, as a function of a pure translational velocity, V_{trans}, for the red blood cells. The V components were $V_{\text{trans},y} = V_{\text{trans},z} = 0$ and $V_{\text{trans},x} = V_{\text{trans}}$. The different markers represent different tissue blood 'volumes' P_{move}, expressed as a probability value (see text). (B) Mean $\langle\omega^0\rangle$ values taken over all possible $V_{\text{trans},x}$ as a function of P_{move}. The vertical bars are the standard deviations.

better evidence of this phenomenon, we presented in figure 3(B) the mean $\langle\omega^0\rangle$ values, taken over all $V_{\text{trans},x}$, as a function of P_{move}.

In figure 4(A) are shown the $\langle\omega^1\rangle$ values of $P(\Delta\omega)$ as a function of a pure translational velocity (i.e. $\langle V^2_{\text{Brown}}\rangle = 0$) for the red blood cells. The $P(\Delta\omega)$ data used to compute $\langle\omega^1\rangle$ were the same as for figure 3, and the different markers correspond to different P_{move}. Again similar to classical laser–Doppler instrumentation, it may be seen that $\langle\omega^1\rangle$ (classically related to the tissue blood flow) increases linearly with increasing $V_{\text{trans},x}$. Increasing P_{move} increases the slope of the $V_{\text{trans},x} - \langle\omega^1\rangle$ relationship. In figure 4(B), we reported the $\langle\omega^1\rangle/\langle\omega^0\rangle$ values as a function of $V_{\text{trans},x}$ (data from figures 3(A) and 4(A)). Classically, the ratio $\langle\omega^1\rangle/\langle\omega^0\rangle$ should be related to the blood velocity only. In this case, it can be seen that the ratio does not fully eliminate the dependence on P_{move}; however, the remaining P_{move} dependence appears to become less important for small $V_{\text{trans},x}$ values.

In figures 5 and 6 are shown the $\langle\omega^0\rangle$ and $\langle\omega^1\rangle$ values for a velocity distribution of the red blood cell components described by equation (7). In this case both $\langle V^2_{\text{Brown}}\rangle$ and $V_{\text{trans},x}$ may be non-nil. It may be seen that the behavior of $\langle\omega^0\rangle$ and $\langle\omega^1\rangle$ is similar to the one appearing in figures 3 and 4. Also in this case, the ratio $\langle\omega^1\rangle/\langle\omega^0\rangle$ does not completely eliminate the dependence on P_{move} (results not shown because the behavior is similar to figure 4(B)).

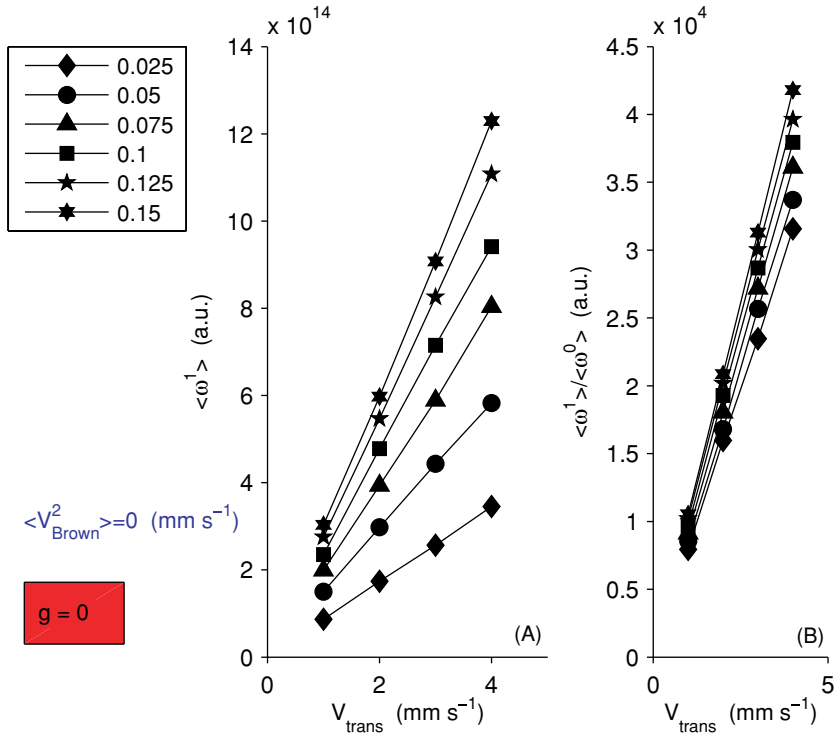

Figure 4. (A) First-order moment, $\langle\omega^1\rangle$, of the FFLDI power spectrum of one representative pixel, $P(\Delta\omega)$, as a function of a pure translational velocity, V_{trans}, for the red blood cells. The $P(\Delta\omega)$ used to obtain $\langle\omega^1\rangle$ were the same as for figure 2. The $\vec{V}$ components were $V_{\text{trans},y} = V_{\text{trans},z} = 0$ and $V_{\text{trans},x} = V_{\text{trans}}$. The different markers represent different tissue blood 'volumes' P_{move}, expressed as a probability value (see text). (B) $\langle\omega^1\rangle/\langle\omega^0\rangle$ values as a function of V_{trans}. The $\langle\omega^1\rangle$ and $\langle\omega^0\rangle$ data have been taken from figures 2(A) and 3(A).

Most interesting, we also studied the same simulations as in figures 5 and 6, but for $g = 0.9$. Note that $g = 0.9$ is representative of the anisotropy parameter of a real biological tissue. Surprisingly enough, figure 7 shows that in this case the P_{move} dependence of $\langle\omega^0\rangle$ is strongly decreased, i.e., there is no influence for large P_{move} values. In practice, this means that in a real biological tissue, $\langle\omega^0\rangle$ is not very sensitive to blood volume changes. However, figure 8 reveals that the velocity sensitivity is still present and that $\langle\omega^1\rangle$ increases linearly as a function of $\langle V^2_{\text{Brown}}\rangle^{1/2}$ for a given $V_{\text{trans},x}$ and P_{move}. The P_{move} dependence of $\langle\omega^1\rangle$ is also still present, and this allows us to interpret $\langle\omega^1\rangle$ as a flow parameter as is the case for the classical laser–Doppler instrumentation.

4. Discussion

In this work, we simulated an ideal FFLDI device by using the Monte Carlo method to describe photon transport into biological tissues and their interaction with moving red blood cells. Presently, no theoretical developments exist for the specific case of FFLDI. Therefore, the proposed simulations try to cover a relatively large spectrum of examples: the case $g = 0$ is rather useful to the study of analytical methods, while the case $g = 0.9$ is much closer to 'real' biological tissues. The sampling rate of the instrument was chosen to cover the frequencies

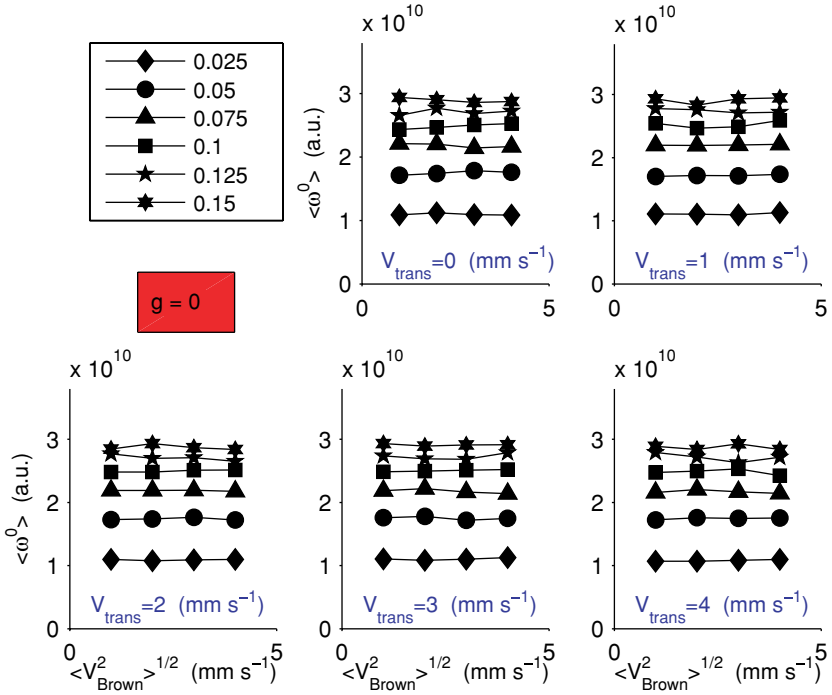

Figure 5. Zero-order moment, $\langle\omega^0\rangle$, of the FFLDI power spectrum of one representative pixel, $P(\Delta\omega)$, as a function of $\langle V^2_{\mathrm{Brown}}\rangle^{1/2}$ and V_{trans}. The $\vec{V}$ components were $V_{\mathrm{trans},y} = V_{\mathrm{trans},z} = 0$ and $V_{\mathrm{trans},x} = V_{\mathrm{trans}}$. The different markers represent different tissue blood 'volumes' P_{move}, expressed as a probability value (see text). The abscissa and ordinate scales are the same for all the graphs.

typically spanned by a real laser–Doppler (bandwidth of 40 KHz). Moreover, a case that takes into account current technological limitations of CMOS detectors was also considered.

It must be noted that only one phase function has been chosen to describe the tissue and that the model can certainly be further improved by including specific functions for the blood and the surrounding tissue. For example, specific phase functions have been derived for *in vitro* blood samples (see e.g. Hammer *et al* 1998, Friebel *et al* 2006). However, it is unclear what is the effect of the red blood cell confinement into the geometrical network of capillaries, arterioles and so on. In fact, inside the vessels the red blood cells may be aligned one after the other; e.g. they may touch each other to form unique elongated shapes. The effect of these and other geometrical constraints on the phase function has not yet been clarified, and should be studied in future. Therefore, we opted for one 'mean' phase function, describing in a reasonable manner a biological tissue.

4.1. Probability density function for the tissue blood velocity

Our simulation model relies on a phenomenological probability density function for $\vec{V}$. Actually, the definition of a suitable analytical representation of $p(\vec{V})$ for a biological tissue (equations (6) and (7)) is a difficult task that should take into account several criteria. As is well known, the geometry of the microvascular tree strongly depends on the tissue type (i.e. muscle, brain, fat, etc) and its high complexity allows one to treat parameters such as $\vec{V}$ in a stochastic manner. In this sense, the probability density function for $\vec{V}$ may potentially have different analytical representations depending on the investigated body region.

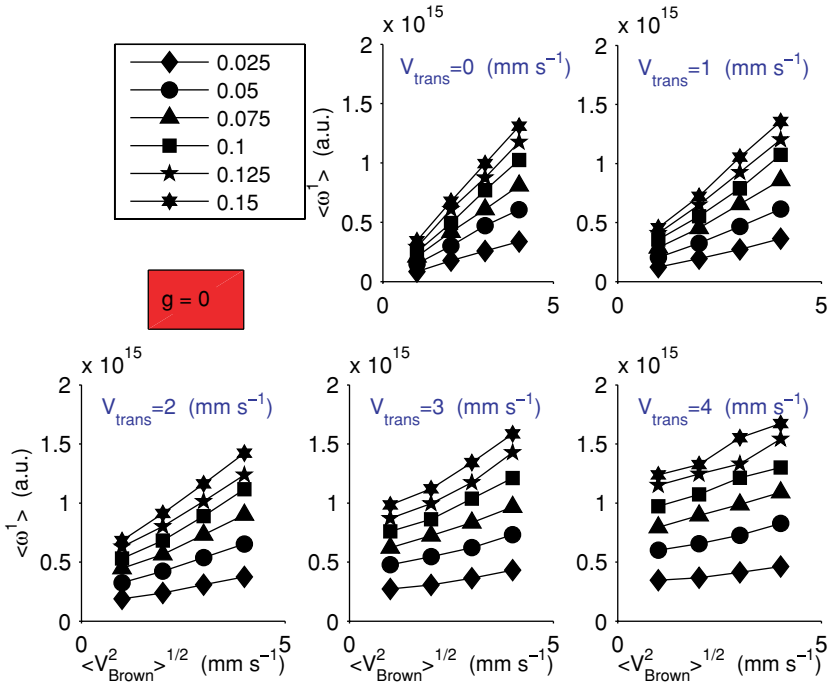

Figure 6. First-order moment, $\langle\omega^1\rangle$, of the FFLDI power spectrum of one representative pixel, $P(\Delta\omega)$, as a function of $\langle V^2_{\mathrm{Brown}}\rangle^{1/2}$ and V_{trans}. The V components were $V_{\mathrm{trans},y} = V_{\mathrm{trans},z} = 0$ and $V_{\mathrm{trans},x} = V_{\mathrm{trans}}$. The different markers represent different tissue blood 'volumes' P_{move}, expressed as a probability value (see text). The abscissa and ordinate scales are the same for all the graphs.

Moreover, a microvascular tree is not an amorphous structure, but it continuously modulates its blood flow/speed through the humoral/neural control of the vascular smooth muscles and precapillary sphincters (Popel and Johnson 2005). The opening and closing of anastomotic microvessels and the modulation of the vascular smooth muscles tone modify the blood velocity and in particular the geometry of the vascular tree. To know whether or not $p(\vec{V})$ remains mathematically the same function during these physiologically induced geometrical changes is not an easy experimental task. Nevertheless, the hypothesis that $p(\vec{V})$ maintains the same analytical form even during blood-flow variations is usually accepted (Bonner and Nossal 1981, Zhong *et al* 1998, Kienle 2001). In fact, this appears to be a reasonable assumption if the number of microvessels in the observed tissue volume is large. This is also the assumption we made here.

The question remains how to define the analytical expression of $p(\vec{V})$. To the best of our knowledge, there are no published data for the *in vivo* probability density functions for V_x, V_y and V_z corresponding to microvascular networks. Data have been reported only for the blood 'speed' ($\|\vec{V}\|$) distribution for different tissues (Klitzman and Johnson 1982, Sarelius 1986, Ellsworth *et al* 1988). Even if an explicit mathematical model was not proposed by these authors, all the experimental measurements show a 'bell shaped' distribution, independent of the tissue type, that may reasonably be described by a function such as $p_n(\|\vec{V}\|)$ (equation (8)). As $p_n(\|\vec{V}\|)$ is derived from $p(\vec{V})$, these experimental data may indirectly motivate the choice of the latter (equation (8)). The large number of measurements (e.g., on large tissue volumes) and the central limit theorem may support the assumption of a Gaussian model such as $p_n(\|\vec{V}\|)$.

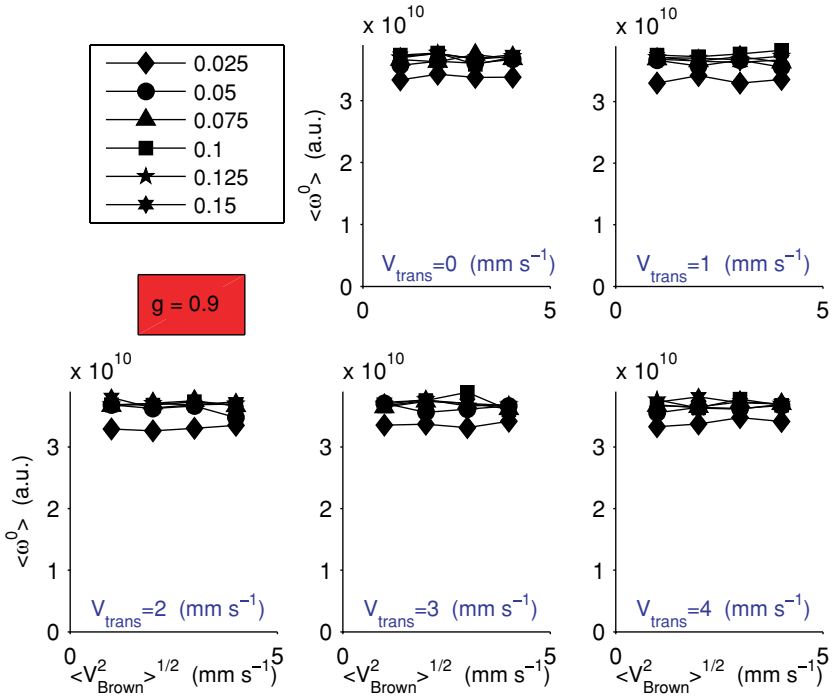

Figure 7. Zero-order moment, $\langle\omega^0\rangle$, of the FFLDI power spectrum of one representative pixel, $P(\Delta\omega)$, as a function of $\langle V^2_{\mathrm{Brown}}\rangle^{1/2}$ and V_{trans}. The $\vec{V}$ components were $V_{\mathrm{trans},y} = V_{\mathrm{trans},z} = 0$ and $V_{\mathrm{trans},x} = V_{\mathrm{trans}}$. The different markers represent different tissue blood 'volumes' P_{move}, expressed as a probability value (see text). The abscissa and ordinate scales are the same for all the graphs. This simulation corresponds to the one in figure 4, however, for the case $g = 0.9$ that better describes a 'real' biological tissue.

Next to the experimental data, many numerical simulations have taken into account different complexity levels of the microvascular blood flow control, and were based on real microvascular geometries (Ellsworth *et al* 1988, Goldman and Popel 1999, 2000, 2001, Ji *et al* 2006, Tsoukias *et al* 2007). With regard to the distribution of $\|\vec{V}\|$, these simulations have reproduced results similar to the experimental data, and thus further motivating the specific choice of $p(\vec{V})$ (equation (8)).

From another point of view, probably one of the most cited contributions related to the laser–Doppler flowmetry is the seminal paper of Bonner and Nossal (1981). Even if this work does not directly deal with imaging, the derived theoretical results (see section 2.4) have been largely utilized as a backbone algorithm of the majority of the laser–Doppler imagers (Serov *et al* 2002, 2005, Serov and Lasser 2005), though the experimental conditions did not satisfy the assumptions of the original paper (e.g., for the FFLDI geometry). While the Bonner and Nossal (1981) approach seems to generate reasonable data, no methodical studies were performed allowing us to demonstrate the validity and the limits of this approach. The important point here is that the $\|\vec{V}\|$ distribution used in the Bonner and Nossal (1981) theoretical derivations corresponds exactly to $p_n(\|\vec{V}\|)$ (equation (8) with $\vec{V}_{\mathrm{trans}} = 0$). For this reason, the use of $p_n(\|\vec{V}\|)$ in the Monte Carlo simulations has also the great advantage of being compatible with the Bonner and Nossal approach when it comes to the definition of the tissue phantom. Based on physiological reasons, Zhong *et al* (1998) have first shown the necessity of using a more general function than that proposed by Bonner and Nossal (1981).

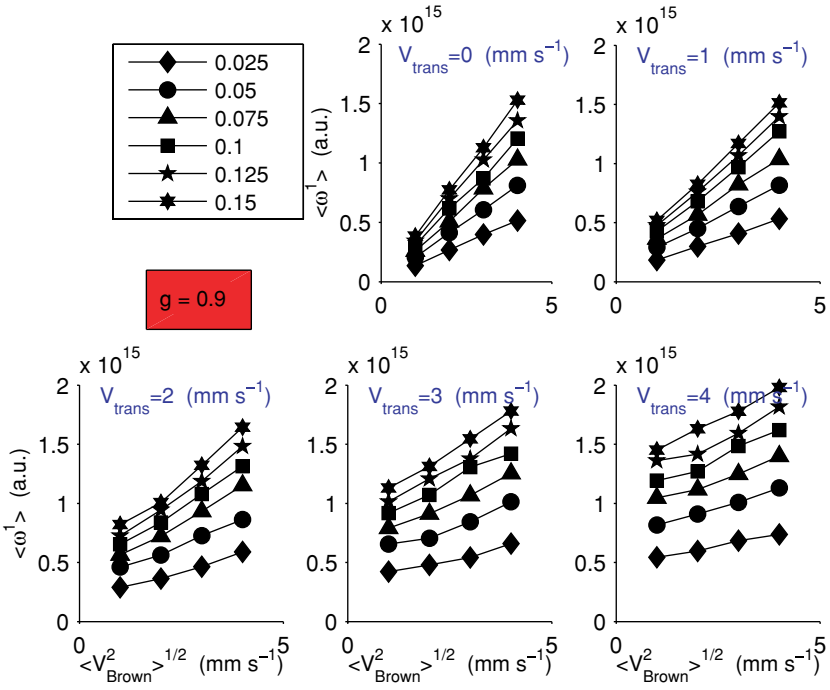

Figure 8. First-order moment, $\langle\omega^1\rangle$, of the FFLDI power spectrum of one representative pixel, $P(\Delta\omega)$, as a function of $\langle V^2_{\mathrm{Brown}}\rangle^{1/2}$ and V_{trans}. The $\bar{V}$ components were $V_{\mathrm{trans},y} = V_{\mathrm{trans},z} = 0$ and $V_{\mathrm{trans},x} = V_{\mathrm{trans}}$. The different symbols represent different tissue blood 'volumes' P_{move}, expressed as a probability value (see text). The abscissa and ordinate scales are the same for all the graphs. This simulation corresponds to the one in figure 5, however, for the case $g = 0.9$ that better describes a 'real' biological tissue.

This was done by introducing the notion of 'bulk' movement for the blood cells. Thus, to take into account this model improvement, in this work also the original condition $\bar{V}_{\mathrm{trans}} = 0$ for $p_n(\|\bar{V}\|)$ has been relaxed.

Of course, if one would like to consider very large vessels, it would probably be necessary to include them explicitly in the geometrical model as small 'tubes'. However, in this case we would no longer be in the condition of having a 'uniform' semi-infinite medium, and this was not the aim of this work. In the case of tissues such as the skin, intermediary solutions may be found for example by explicitly distinguishing a finite number of well-defined speed and vessel sizes included in the same investigated tissue volume (Fredriksson *et al* 2008).

In conclusion, the current form of $p(\bar{V})$ is probably the only one that allows us to obtain explicit analytical solutions in the standard laser–Doppler flowmetry (Binzoni *et al* 2004, 2006) and that at the same time is reasonably compatible with the underlying muscle physiology. The derivation of new analytical models for FFLDI with more complex geometries will probably be based on a similar choice, and remains a topic for future research.

4.2. Physiological interpretation of the zero- and first-order moments

The most intriguing result of this work is probably the observation that FFLDI has no or very poor sensitivity to tissue blood volume variations (figure 7). While classical laser–Doppler flowmeters (LDF) can easily follow P_{move} changes through the monitoring of $\langle\omega^0\rangle$, this is not

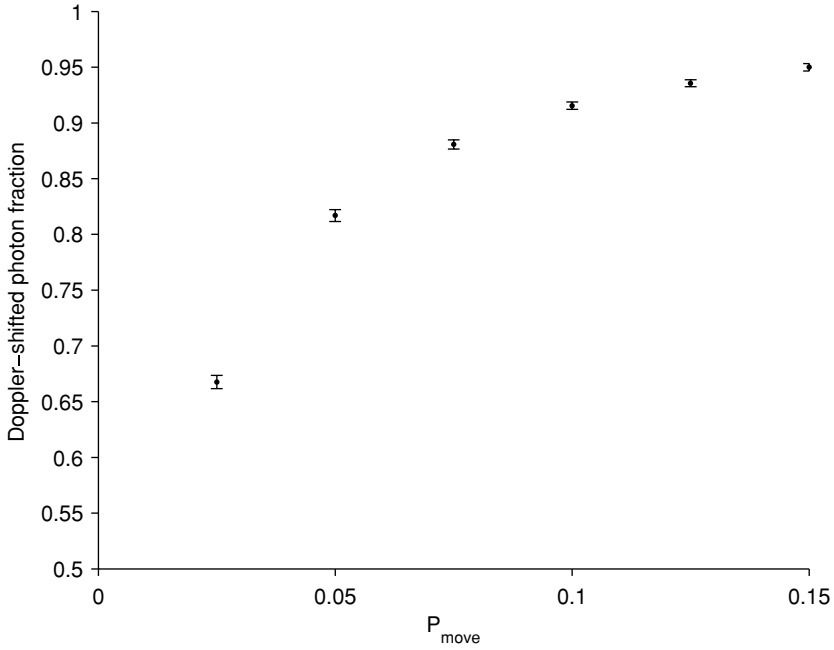

Figure 9. Fraction of photons that reach the photodetector and that are Doppler shifted, for the FFLDI geometry, as a function of the blood 'volume' (P_{move}), expressed as a probability value (see section 2.2). The vertical bars represent standard deviations.

valid anymore for FFLDI (except for very low P_{move} values, see below). The reason of this behavior appears to be due to the fact that biological tissues strongly forward scatter the light. Indeed, the sensitivity of $\langle\omega^0\rangle$ to P_{move} variations is readily regained if the anisotropy parameter g is reduced to zero (figure 5). One must not forget that a high tissue blood concentration and a low μ_s' (long photon path lengths before detection) might cause virtually all photons to become Doppler shifted. Serov *et al* (2000) have demonstrated (at a 1, 2 mm interoptode distance) that skin measurements already display a fraction of Doppler shifted photons of about 0.5 for the arm and 0.7 for the finger (fiber separation: 1.2 mm). In our case, as it should be for the FFLDI configuration, figure 9 shows that this fraction is higher and that the curve tends to saturate for increasing P_{move} values. This could also explain the low sensitivity of FFLDI for a large P_{move}.

In practice, FFLDI can only follow global tissue blood flow changes by monitoring $\langle\omega^1\rangle$. This means that $\vec{V}$ cannot be extracted from the total flow, as it is usually done in classical LDF by the ratio $\langle\omega^1\rangle/\langle\omega^0\rangle$. In other words, it is not possible to decide if a flow variation is due to a change in the tissue blood volume (P_{move}), velocity ($\vec{V}$) or a combination of both. Moreover, $\vec{V}$ depends itself on two factors, $\left\langle V^2_{\text{Brown}}\right\rangle^{1/2}$ and $\vec{V}_{\text{trans}}$, and this further complicates the physiological interpretation of $\langle\omega^1\rangle$. One possible solution to this problem could be to develop an analytical model that exploits the complete information of $P(\Delta\omega)$ to obtain P_{move}, $\left\langle V^2_{\text{Brown}}\right\rangle^{1/2}$ and $\vec{V}_{\text{trans}}$, as has been done in the laser–Doppler flowmetry before (Boas 1996, Binzoni *et al* 2006). As explained in the 'Introduction' section, the derivation of an analytical model depends on our capability to describe the photon migration into the tissue simultaneously for very short and very large source–detector distances. For the sake of completeness, in figure 10, we show an example where the optical spectrum, $W_{\text{tot}}(\omega)$, is split

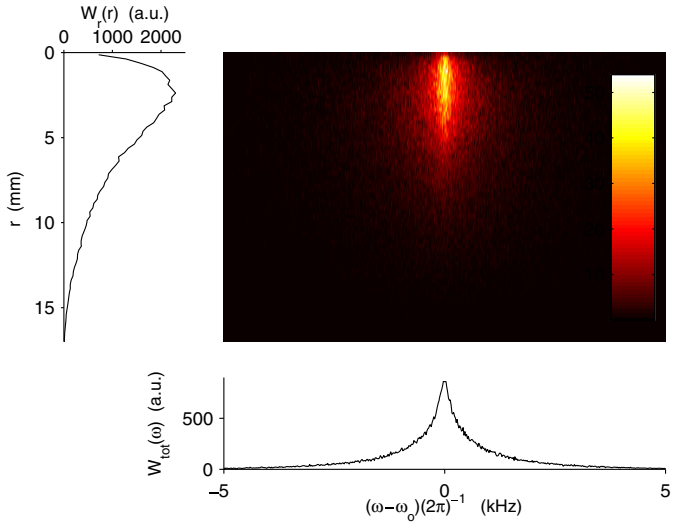

Figure 10. The colored image represents the intensities values of the optical spectrum, $W_{\omega,r}(\omega, r)$, decomposed as a function of the distance, r, existing between the position of the starting point of each photon packet and the respective detection point. The function $W_{\text{tot}}(\omega)$ is the sum of all the lines of the 2D image, and $W_r(r)$ is the sum of all the columns. The $\omega - \omega_0$ and r scales also hold for the 2D image. The parameters for the simulation were $g = 0.9$, $\langle V^2_{\text{Brown}}\rangle^{1/2} = 1$ mm s^{-1}, $V_{\text{trans},y} = V_{\text{trans},z} = 0$ mm s^{-1}, $V_{\text{trans},x} = 1$ mm s^{-1}, $P_{\text{move}} = 0.075$.

as a function of r (mm), the distance between the positions of the entrance and detection points of a photon packet. The resulting 2D histogram $W_{\omega,r}(\omega, r)$ is shown in figure 10, where the colors represent the different intensities of $W_{\omega,r}(\omega, r)$. The graphs appearing near the axis are the marginalized histograms of $W_{\text{tot}}(\omega, r)$:

$$W_{\text{tot}}(\omega) = \int_0^\infty W_{\omega,r}(\omega, r)\,\mathrm{d}r \tag{12}$$

and

$$W_r(r) = \int_0^\infty W_{\omega,r}(\omega, r)\,\mathrm{d}\omega. \tag{13}$$

The significance of $W_r(r)$ is that the major fraction of the photons reaching the detection pixel entered the tissue at a distance larger than ∼2 mm. This is not very far, but it could justify an approximation of the radiative transport equation allowing us to facilitate the analytical derivations. The specific behavior of $W_r(r)$ as a function of r is mainly influenced by the anisotropy factor g; i.e., low g values will fill the photon lack in the range 0–2 mm (not shown), a situation that is not present in a real biological tissue. It is important to emphasize that the behavior $W_r(r)$ in figure 10 does not indicate that the information content of the signal (the tissue blood flow) is dominated by tissue regions far from the detection point (>2 mm). In fact, we have previously demonstrated (Binzoni *et al* 2008a) that blood volume and/or velocity information mainly originates from a region situated just under the detection point in the case of an FFLDI source–detector geometry. This might also explains why FFLDI allows us to obtain a coherent image of the tissue blood perfusion occurring under the tissue surface. It is in this sense that $\langle\omega^0\rangle$ and $\langle\omega^1\rangle$ must be interpreted.

As noted before, a method based on direct fitting of $P(\Delta\omega)$ would exploit the full spectrum; however, this would be impractical for real-time imaging. In fact, for an image of

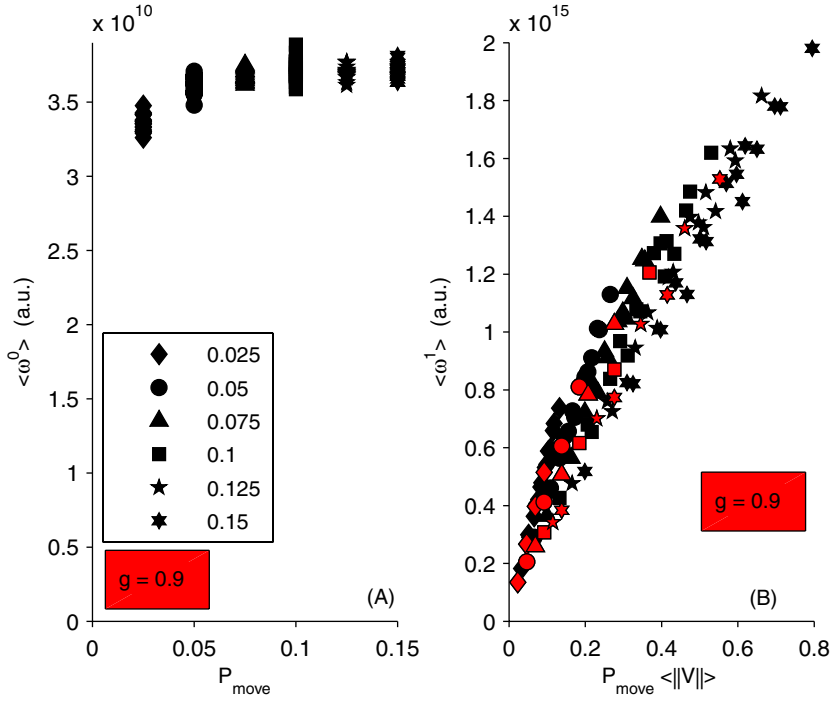

Figure 11. The spectrum $P(\Delta\omega)$ utilized to compute $\langle\omega^0\rangle$ and $\langle\omega^1\rangle$ in this figure are the same as in figures 6 and 7. (A) Zero-order moment, $\langle\omega^0\rangle$, of the FFLDI power spectrum of one representative pixel, $P(\Delta\omega)$, as a function of the tissue blood 'volumes' P_{move}, expressed as a probability value (see text). The different markers represent different tissue blood 'volumes' P_{move} and also hold for figure (B). (B) First-order moment, $\langle\omega^1\rangle$, of the FFLDI power spectrum of one representative pixel, $P(\Delta\omega)$, as a function of the *mean* tissue blood 'flow', $P_{\text{move}}\langle\|\vec{V}\|\rangle$, expressed in arbitrary units. The parameter $\langle\|\vec{V}\|\rangle$ is computed using equation (14). The symbols colored in red have a $\vec{V}_{\text{trans}} = 0$ value. The necessary computation time on an eight-node cluster to obtain the data appearing in this figure corresponds to 74 days.

size 256 × 256 pixels, we must be able to perform 65 536 fitting procedures in real time! For this reason, we investigate the usefulness of a well-chosen approximation. Specifically, let us express the tissue blood flow as the product of the blood 'volume' times the *mean* red blood cells speed. This means that the blood flow must be proportional to $P_{\text{move}}\langle\|\vec{V}\|\rangle$, where $\langle\ \rangle$ is the mean expected value. The idea is that $P_{\text{move}}\langle\|\vec{V}\|\rangle$ must as a first approximation be linearly related to $\langle\omega^1\rangle$ (and $\langle\omega^1\rangle$ is easy and fast to compute). The parameter $\langle\|\vec{V}\|\rangle$ is obtained from equation (8) as

$$\langle\|\vec{V}\|\rangle = \int_0^\infty \|\vec{V}\| p_n(\|\vec{V}\|) d\|\vec{V}\| = \frac{\sqrt{6}}{3}\frac{\langle V^2_{\text{Brown}}\rangle^{1/2}}{\sqrt{\pi}} e^{-\frac{3}{2}\frac{\|\vec{V}_{\text{trans}}\|^2}{\langle V^2_{\text{Brown}}\rangle}} + \left(\|\vec{V}_{\text{trans}}\| + \frac{\langle V^2_{\text{Brown}}\rangle}{3\|\vec{V}_{\text{trans}}\|}\right) \text{erf}\left(\frac{\sqrt{6}}{2}\frac{\|\vec{V}_{\text{trans}}\|}{\langle V^2_{\text{Brown}}\rangle^{1/2}}\right). \tag{14}$$

It is interesting to note that for $\vec{V}_{\text{trans}} = 0$:

$$\langle\|\vec{V}\|\rangle = \frac{2\sqrt{6}}{3}\frac{\langle V^2_{\text{Brown}}\rangle^{1/2}}{\sqrt{\pi}}, \tag{15}$$

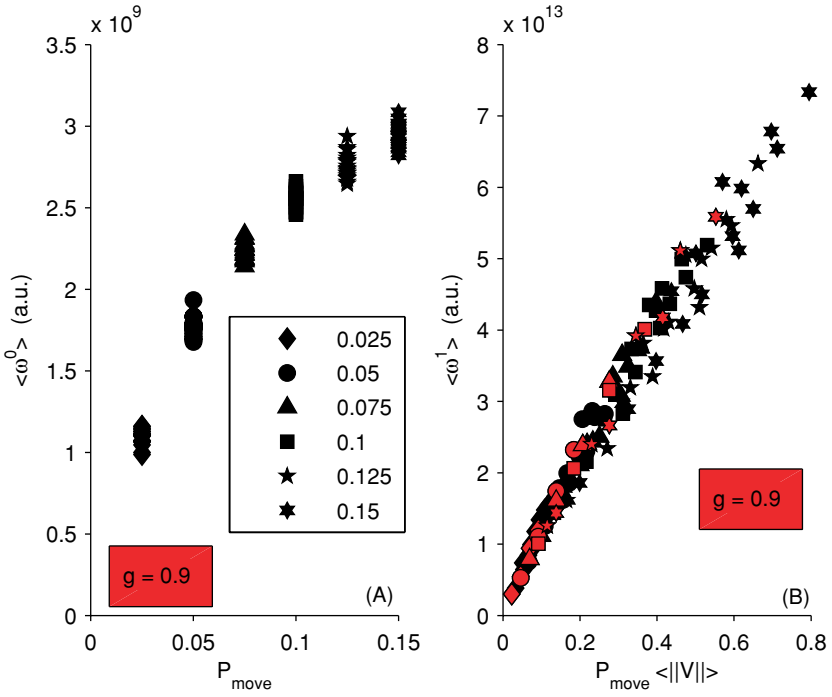

Figure 12. (A) Zero-order moment, $\langle\omega^0\rangle$, of the 'classical' LDF power spectrum as a function of the tissue blood 'volumes' P_{move}, expressed as a probability value (see section 2.2). The different markers represent different tissue blood 'volumes' P_{move} and also hold for (B). (B) First-order moment, $\langle\omega^1\rangle$, of the 'classical' LDF power spectrum as a function of the *mean* tissue blood 'flow', $P_{\mathrm{move}}\langle\|\vec{V}\|\rangle$, expressed in arbitrary units. The parameter $\langle\|\vec{V}\|\rangle$ is computed using equation (14). The symbols colored in red have a $\vec{V}_{\mathrm{trans}} = 0$ value.

and in the case of the classical Bonner and Nossal (1981) laser–Doppler approximation this is proportional to $\langle\omega^1\rangle/\langle\omega^0\rangle \propto \langle\|\vec{V}\|\rangle$. By using equation (14), the data presented in figures 7 and 8 may now be expressed in a new form. From figure 11, it clearly appears that $\langle\omega^0\rangle$ is insensitive to P_{move} changes, especially for values $P_{\mathrm{move}} \geqslant 0.05$. However, the parameter $\langle\omega^1\rangle$ is linearly related to $P_{\mathrm{move}}\langle\|\vec{V}\|\rangle$ only if P_{move} is not submitted to large variations. These results are nicely compatible with *in vitro* measurements realized by Serov *et al* (2005) with FFLDI and in 'one-pixel detection mode' (one-pixel detection mode allows a high acquisition rate respecting the Shannon's sampling theorem, see below). The red markers in figure 11 (gray, in the non-electronic version of the manuscript) represent $\langle\omega^1\rangle$ values for which $\vec{V}_{\mathrm{trans}} = 0$. It can be seen that $\vec{V}_{\mathrm{trans}}$ has not a large influence on the total range of possible *mean* blood 'flows', $P_{\mathrm{move}}\langle\|\vec{V}\|\rangle$. However, we must not forget that $\vec{V}_{\mathrm{trans}}$ is of great physiological importance because some tissues have an oriented microvascular network, as in the muscle or the brain. In this type of tissue, a situation where $\vec{V}_{\mathrm{trans}} = 0$ corresponds to the mean velocity $\langle\vec{V}\rangle = 0$ (note that $\langle\|\vec{V}\|\rangle \neq \langle\vec{V}\rangle$), and thus to the fact that there is no net oxygen and/or blood flow into the tissue. The consequence is that when $\vec{V}_{\mathrm{trans}} = 0$, the tissue is physiologically not viable.

In vivo it is practically impossible that the blood volume, for a given tissue (e.g. muscle), changes drastically from 0.025 to 0.15, and thus we can assume that the $P_{\mathrm{move}}\langle\|\vec{V}\|\rangle - \langle\omega^1\rangle$ relationship is linear and that $\langle\omega^1\rangle$ may be utilized to monitor tissue blood flow changes.

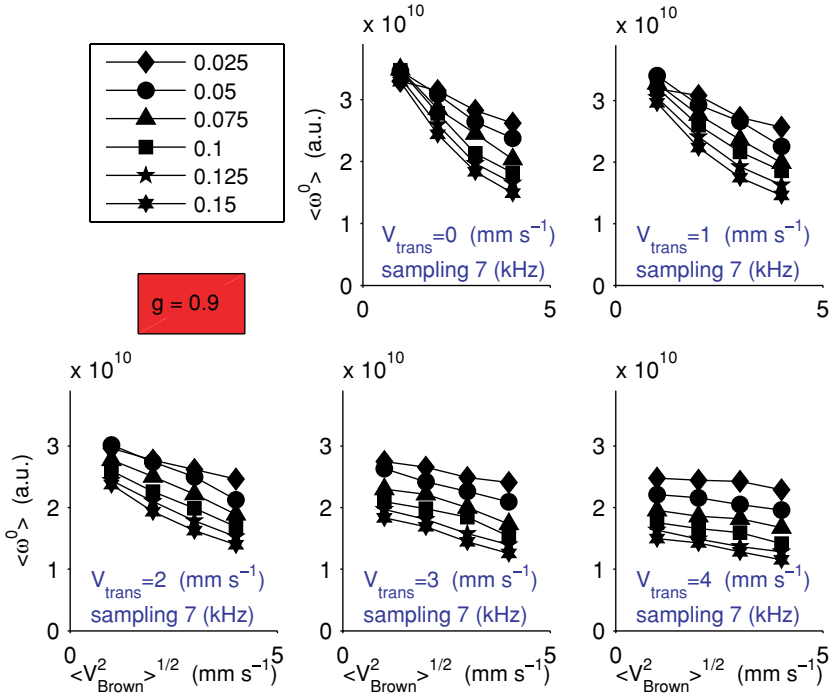

Figure 13. Zero-order moment, $\langle\omega^0\rangle$, of the FFLDI power spectrum of one representative pixel, $P(\Delta\omega)$, as a function of $\langle V^2_{\text{Brown}}\rangle^{1/2}$ and V_{trans}. The $\bar{V}$ components were $V_{\text{trans},y} = V_{\text{trans},z} = 0$ and $V_{\text{trans},x} = V_{\text{trans}}$. The different markers represent different tissue blood 'volumes' P_{move}, expressed as a probability value (see section 2.2). The abscissa and ordinate scales are the same for all the graphs. The sampling rate was 7 kHz.

However, $\langle\omega^1\rangle$ must always be considered with care because, even if the error is small, to a single $\langle\omega^1\rangle$ value always correspond a range of possible $P_{\text{move}}\langle\|\bar{V}\|\rangle$ values. This situation is probably slightly improved for some tissues that have g larger than 0.9, but this will not eliminate the problem. In conclusion, the representation of figure 11 for $\langle\omega^1\rangle$ slightly improves its physiological interpretation, but does not exclude the necessity to develop in the future new faster and precise FFLDI algorithms. In this context, fast algorithms obtained with an approach different from laser–Doppler (laser speckle imaging) and applicable to the FFLDI geometry have been considered, for example, among others by Briers (2001), Durduran *et al* (2004), Briers (2007). Such algorithms allow in principle to circumvent the problems created by Shannon's sampling theorem and the limited sampling rate of the detectors. Unfortunately, the simulations necessary to investigate these algorithms are different from the present ones and a direct comparison appears to be difficult, but certainly deserves future attention.

To better depict the different significance of the moments for 'classical' LDF and FFLDI, figure 12 explicitly shows the results of the Monte Carlo simulations for the former. As explained in the previous sections, figure 12 clearly confirms that in the 'classical' LDF, $\langle\omega^0\rangle$ is highly sensitive to P_{move}, and this is why $\langle\omega^0\rangle$ is usually utilized to estimate blood volume changes (a shorter interoptode spacing, e.g. 0.25 mm, would further improve the linear behavior observed in figure 12(A)). However, when comparing figure 12 and 11, we clearly see that for FFLDI this is no longer the case. Thus, in practice the algorithm developed for 'classical' LDF works only partially well if applied to FFLDI.

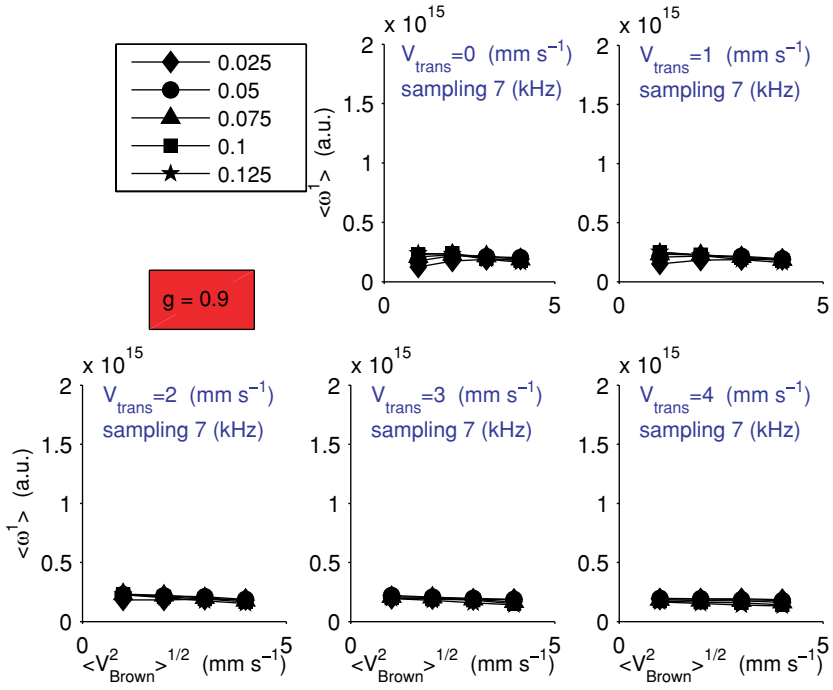

Figure 14. First-order moment, $\langle\omega^1\rangle$, of the FFLDI power spectrum of one representative pixel, $P(\Delta\omega)$, as a function of $\langle V^2_{\mathrm{Brown}}\rangle^{1/2}$ and V_{trans}. The V components were $V_{\mathrm{trans},y} = V_{\mathrm{trans},z} = 0$ and $V_{\mathrm{trans},x} = V_{\mathrm{trans}}$. The different markers represent different tissue blood 'volumes' P_{move}, expressed as a probability value (see section 2.2). The abscissa and ordinate scales are the same for all the graphs. The sampling rate was 7 kHz.

4.3. Implications for the experimentalist

Our results also have important implications for the FFLDI experimentalist. In particular, the use of CMOS detectors for FFLDI brings along the trade-off between spatial and temporal resolutions. Specifically, the larger the image size, the slower the sampling rate. In fact, the high-frequency content of $P(\Delta\omega)$ becomes stronger as $\vec{V}$ and P_{move} increase (however, the overall behavior of the spectrum is very difficult to predict intuitively, and for this reason it is necessary to perform simulations). A too low temporal sampling rate will miss high-frequency components and introduce distortions in the $\langle\omega^0\rangle$ and $\langle\omega^1\rangle$ estimation. Often, the trade-off can be tuned by the user. For this reason, it is essential to understand the effect of undersampling on the estimated $\langle\omega^0\rangle$ and $\langle\omega^1\rangle$, and to see the consequences on the physiological interpretation of these parameters. In figures 13 and 14, we have reported the same simulations such as those in figures 7 and 8 but where we have used an upper cutoff of 3500 Hz on $P(\Delta\omega)$ (equivalent to a sampling rate of 7000 Hz), before the calculation of $\langle\omega^0\rangle$ and $\langle\omega^1\rangle$. This simulates a possible low sampling rate of the CMOS for a large field-of-view (Serov *et al* 2002, 2005, Serov and Lasser 2005). Figures 13 and 14 reveal surprising behavior: blood flow is more or less constant when $\vec{V}$ actually increases at a constant P_{move} (figure 14). Further on, $\langle\omega^0\rangle$ also leads to wrong interpretations because it decreases for increasing $\vec{V}$ without any physiological meaning (figure 13). Figure 15 is the equivalent of figure 11, but with the presence of the cutoff, and explicitly shows that the linear relationship between flow and $\langle\omega^1\rangle$ in this case is broken. The effect of the cutoff might even become worse for a larger g due to the deeper

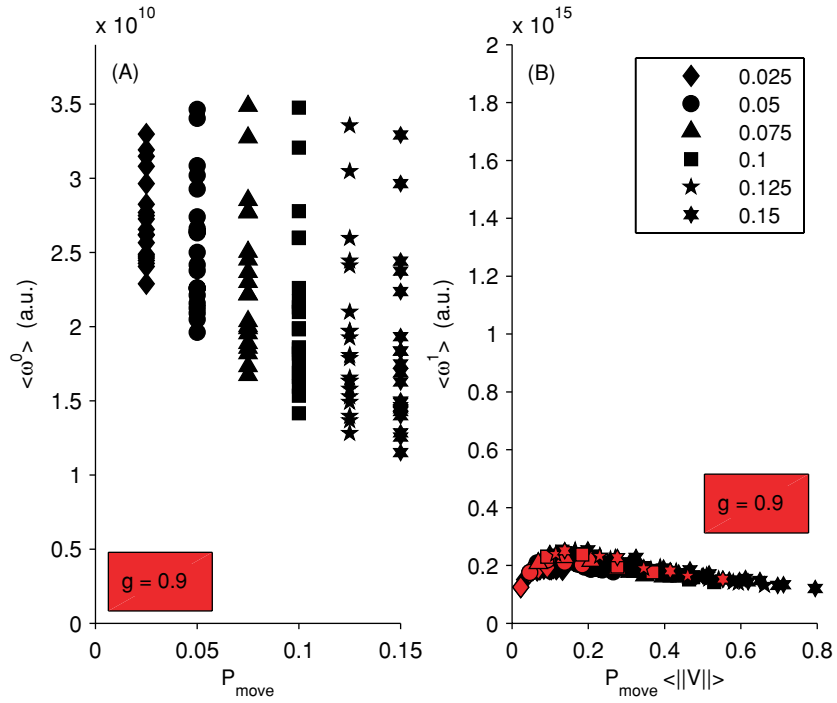

Figure 15. Equivalent figure to figure 9 where the sampling rate of the full-field imager is 7 kHz. (A) Zero-order moment, $\langle\omega^0\rangle$, of the FFLDI power spectrum of one representative pixel, $P(\Delta\omega)$, as a function of the tissue blood 'volumes' P_{move}, expressed as a probability value (see section 2.2). The different symbols represent different tissue blood 'volumes' P_{move} and also hold for (B). (B) First-order moment, $\langle\omega^1\rangle$, of the FFLDI power spectrum of one representative pixel, $P(\Delta\omega)$, as a function of the *mean* tissue blood 'flow', $P_{\text{move}}\langle\|\vec{V}\|\rangle$, expressed in arbitrary units. The parameter $\langle\|\vec{V}\|\rangle$ is computed using equation (14). The symbols colored in red have a $\vec{V}_{\text{trans}} = 0$ value.

penetration of the photons at the beginning of the photon path and thus to the accumulation of a larger Doppler shift at the detector level (a similar effect that was observed when increasing $g = 0$ to $g = 0.9$).

5. Conclusions

The contributions of this paper were made possible using a Monte Carlo simulation for FFLDI, which is to the best of our knowledge the first attempt in this domain that takes into account the specific setting of full-field imaging. We have demonstrated that FFLDI is a promising method for real-time blood flow monitoring. However, the interpretation of the zero- and first-order moments should be handled with care, as these quantities are differently linked to the underlying physiological parameters than in the classical laser–Doppler flowmetry. Due to strong forward scattering in a biological tissue, the zero-order moment $\langle\omega^0\rangle$ in FFLDI has poor sensitivity to blood volume changes. The first-order moment $\langle\omega^1\rangle$ does vary with blood flow variations, but we cannot separate blood volume from velocity changes. We also discussed various topics for future research, such as the development of analytical models for spectrum fitting procedures. Finally, we showed that the (temporal) sampling rate could strongly influence the moment estimation; e.g., a too low sampling rate could let vary $\langle\omega^1\rangle$

and blood flow in opposite ways. This is an important consideration for both the hardware designer, when setting the camera specifications, and the experimentalist, when tuning the resolution-sampling rate trade-off.

Acknowledgments

The authors would like to thank the 'Faculté de Médecine' of Geneva for the Mimosa grant that allowed the computer cluster to be set up. This work was also supported in part (second author, DVDV) by the CIBM.

References

Binzoni T, Leung T S, Giust R, Rüfenacht D and Gandjbakhche A H 2008a Light transport in tissue by 3D Monte Carlo: influence of boundary voxelization *Comput. Methods Programs Biomed.* **89** 14–23

Binzoni T, Leung T S, Rüfenacht D and Delpy D T 2006 Absorption and scattering coefficient dependence of laser–Doppler flowmetry models for large tissue volumes *Phys. Med. Biol.* **51** 311–33

Binzoni T, Leung T S, Seghier M L and Delpy D T 2004 Translational and Brownian motion in laser–Doppler flowmetry of large tissue volumes *Phys. Med. Biol.* **49** 5445–58

Binzoni T, Vogel A, Gandjbakhche A H and Marchesini R 2008b Detection limits of multi-spectral optical imaging under the skin surface *Phys. Med. Biol.* **53** 617–36

Boas D A 1996 Diffusive photons probes of structural and dynamical properties of turbid media: theory and biomedical applications *PhD Thesis* University of Pensilvania

Bonner R and Nossal R 1981 Model for laser Doppler measurements of blood-flow in tissue *Appl. Opt.* **20** 2097–107

Briers J D 2001 Laser Doppler, speckle and related techniques for blood perfusion mapping and imaging *Physiol. Meas.* **22** R35–66

Briers J D 2007 Laser speckle contrast imaging for measuring blood flow *Opt. Appl.* **37** 139–52

Courvoisier C 2006 Etude d'un continuum de lumire en régime femtoseconde. Applications au domaine biologique: microscopie et spectroscopie en temps résolu *PhD Thesis* University of Besançon, France

De Mul F F M, Koelink M H, Kok M L, Harmsma P J, Greve J, Graaff R and Aarnoudse J G 1995 Laser Doppler velocimetry and Monte Carlo simulations on models for blood perfusion in tissue *Appl. Opt.* **34** 6595–611

Durduran T, Burnett M G, Yu G, Zhou C, Furuya D, Yodh A G, Detre J A and Greenberg J H 2004 Spatiotemporal quantification of cerebral blood flow during functional activation in rat somatosensory cortex using laser-speckle flowmetry *J. Cereb. Blood Flow Metab.* **24** 518–25

Ellsworth M L, Popel A S and Pittman R N 1988 Assessment and impact of heterogeneities of convective oxygen transport parameters in capillaries of striated muscle: experimental and theoretical *Microvasc. Res.* **35** 341–62

Forrester A T 1961 Photoelectric mixing as a spectroscopic tool *J. Opt. Soc. Am.* **51** 253–9

Fossum E R 1997 CMOS image sensors: electronic camera-on-a-chip *IEEE Trans. Electron. Devices* **44** 1689–98

Fredriksson I, Larsson M and Stršmberg T 2008 Optical microcirculatory skin model: assessed by Monte Carlo simulations paired with *in vivo* laser Doppler flowmetry *J. Biomed. Opt.* **13** 014015

Friebel M, Roggan A, Müller G and Meinke M 2006 Determination of optical properties of human blood in the spectral range 250 to 1100 nm using Monte Carlo simulations with hematocrit-dependent effective scattering phase functions *J. Biomed. Opt.* **11** 34021

Goldman D and Popel A S 1999 Computational modeling of oxygen transport from complex capillary networks. Relation to the microcirculation physiome *Adv. Exp. Med. Biol.* **471** 555–63

Goldman D and Popel A S 2000 A computational study of the effect of capillary network anastomoses and tortuosity on oxygen transport *J. Theor. Biol.* **206** 181–94

Goldman D and Popel A S 2001 A computational study of the effect of vasomotion on oxygen transport from capillary networks *J. Theor. Biol.* **209** 189–99

Hammer M, Schweitzer D, Michel B, Thamm E and Kolb A 1998 Single scattering by red blood cells *Appl. Opt.* **37** 7410–8

Henyey L G and Greenstein J L 1941 Diffuse radiation in the galaxy *Astrophys. J.* **93** 70–83

Hoffman A, Loose M and Suntharalingam V 2005 CMOS detector technology *Exp. Astron.* **19** 111–34

Ji J W, Tsoukias N M, Goldman D and Popel A S 2006 A computational model of oxygen transport in skeletal muscle for sprouting and splitting modes of angiogenesis *J. Theor. Biol.* **241** 94–108

Kienle A 2001 Non-invasive determination of muscle blood flow in the extremities from laser Doppler spectra *Phys. Med. Biol.* **46** 1231–44

Kirkby D R and Delpy D T 1997 Parallel operation of Monte Carlo simulations on a diverse network of computers *Phys. Med. Biol.* **42** 1203–8

Klitzman B and Johnson P C 1982 Capillary network geometry and red cell distribution in hamster cremaster muscle *Am. J. Physiol.* **242** H211–9

Liebert A, Zolek N and Maniewski R 2006 Decomposition of a laser–Doppler spectrum for estimation of speed distribution of particles moving in an optically turbid medium: Monte Carlo validation study *Phys. Med. Biol.* **51** 5737–51

Liebert A, Zolek N, Wojtkiewicz S and Maniewski R 2007 Estimation of speed distribution of particles moving in an optically turbid medium using decomposition of a laser–Doppler spectrum *Conf. Proc. IEEE Eng. Med. Biol. Soc. 2007* pp 4080–2

Popel A S and Johnson P C 2005 Microcirculation and hemorheology *Ann. Rev. Fluid Mech.* **37** 43–69

Prahl S A, Keijzer M, Jacques S L and Welch A J 1989 A Monte Carlo code of light propagation in tissue *Proc. SPIE* **5** 102–11

Sarelius I H 1986 Distribution of red blood cell flow in capillary networks *Microvascular Networks: Experimental and Theoretical Studies* ed A S Popel and P C Johnson (Basel: Karger) pp 77–88

Serov A, Steenbergen W and de Mul F 2000 A method for estimation of the fraction of Doppler-shifted photons in light scattered by mixture of moving and stationary scatterers *Proc. SPIE* **4001** 178–89

Serov A, Steenbergen W and de Mul F 2002 Laser Doppler perfusion imaging with a complimentary metal oxide semiconductor image sensor *Opt. Lett.* **27** 300–2

Serov A, Steinacher B and Lasser T 2005 Full-field laser Doppler perfusion imaging and monitoring with an intelligent CMOS camera *Opt. Express* **13** 3681–9

Serov A and Lasser T 2005 High-speed laser Doppler perfusion imaging using an integrating CMOS image sensor *Opt. Express* **13** 6416–28

Sobol I M 1975 *The Monte Carlo Method* (Moscow: Mir)

Soelkner G, Mitic G and Lohwasser R 1997 Monte Carlo simulations and laser Doppler flow measurements with high penetration depth in biological tissuelike head phantoms *Appl. Opt.* **36** 5647–54

Torricelli A, Quaresima V, Pifferi A, Biscotti G, Spinelli L, Taroni P, Ferrari M and Cubeddu R 2004 Mapping of calf muscle oxygenation and haemoglobin content during dynamic plantar flexion exercise by multi-channel time-resolved near-infrared spectroscopy *Phys. Med. Biol.* **49** 685–99

Tsoukias N M, Goldman D, Vadapalli A, Pittman R N and Popel A S 2007 A computational model of oxygen delivery by hemoglobin-based oxygen carriers in three-dimensional microvascular networks *J. Theor. Biol.* **248** 657–74

Vennemann P, Lindken R and Westerweel J 2007 *In vivo* whole-field blood velocity measurement techniques *Exp. Fluids* **42** 495–511

Wang L, Jacques S L and Zheng L 1995 MCML – Monte Carlo modeling of light transport in multi-layered tissues *Comput. Methods Programs Biomed.* **47** 131–46

Witt A N 1977 Multiple scattering in reflection nebulae: I. A Monte Carlo approach *Astrophys. J.* **35** S1–S6

Zaccanti G, Taddeucci A, Barilli M, Bruscaglioni P and Martelli F 1995 Optical properties of biological tissues *Proc. SPIE* **2389** 513–21

Zhong J, Seifalian A M, Salerud G E and Nilsson G E 1998 A mathematical analysis on the biological zero problem in laser Doppler flowmetry *IEEE Trans. Biomed. Eng.* **45** 354–64